SUPPLEMENTARY INFORMATION

Reactions of Fluid and Lattice Oxygen Mediated by Interstitial Atoms at the TiO_2 (110)-Water Interface

Heonjae Jeong[b,c], Ian I. Suni[a], Raylin Chen[a], Marina Miletic[a], Xiao Su[a] and Edmund G. Seebauer[a]*

[a] Department of Chemical and Biomolecular Engineering, University of Illinois at Urbana-Champaign, Urbana, Illinois 61801, United States

[b] Department of Mechanical Science and Engineering, University of Illinois at Urbana-Champaign, Urbana, Illinois 61801, United States

[c] Department of Electronic Engineering, Gachon University, Seongnam, Gyeonggi 13120, South Korea

* Corresponding author, eseebaue@illinois.edu

1. Method for determination of profile metrics

The metrics W and C_{min} associated with fractionation could be determined by straightforward visual inspection of the profiles. However, the decay constants λ_1 and λ_2, along with the net injection flux F_{18} of ^{18}O, required more sophisticated methods because λ_2 was usually much larger than the depth to which SIMS measurements extended.

Determination of the decay constants exploited the fact that decay of the ^{18}O concentration beyond the peak obeyed a bi-exponential functional form having two widely separated decay constants, with $\lambda_1 << \lambda_2$. A practical consequence was that λ_1 dominated the change in ^{18}O concentration near the peak, and λ_2 dominated at depths several times λ_1 from the peak. In other words, the profile decayed according to λ_1 down to an approximate plateau, followed by a much slower decay according to λ_2. The plateau was typically 3-10% higher than the ^{18}O natural abundance concentration C_O of 1.276×10^{20} cm^{-3}, with larger values occurring at higher temperatures. In each profile, the concentration characterizing this plateau was normalized with respect to C_O to yield a dimensionless scaling factor Z, which typically varied from 1.03 to 1.1. Thus, a functional form derived previously[1] for ^{18}O injection from a surface was adapted to phenomenologically describe the λ_1 region according to:

$$C(x) = C_O\left[\frac{C_{OT}-C_O}{C_o}e^{-\frac{x}{\lambda_1}+b1} + Z\right] \quad \text{(S1)},$$

where C denotes the concentration of ^{18}O at depth x from the surface, C_{OT} is the total concentration of O atoms in the lattice (6.38×10^{22} cm^{-3}), and b_1 is a phenomenological amplitude factor. In the λ_2 region, C continued to decay to the natural abundance baseline ($Z \equiv 1$) according to a similar adaptation:

$$C(x) = C_O\left[\frac{C_{OT}-C_O}{C_O}e^{-\frac{x}{\lambda_2}+b2} + 1\right] \quad \text{(S2)},$$

where b_2 is a second phenomenological amplitude factor.

Eq. (S1) was fitted to the λ_1 region of the profile using a nonlinear least squares algorithm to determine λ_1, b_2 and Z. The range of depths contributing to the fit lay between $x=\alpha$, which is near the peak (determined as described below), and the lesser of either $\alpha+4\lambda_1$ or the maximum depth to which the SIMS profile extended. For a profile that extended very deep, the fitting process was iterated to ensure self-consistency between the value of λ_1 and the depth $\alpha+4\lambda_1$ used as a boundary of the fitting region. When referenced to C_O, C declines at $\alpha+4\lambda_1$ to only about 2% of its maximum near the peak. Thus, the value of λ_1 exhibits little sensitivity to the exact choice of the deeper boundary. Rarely were more than two iterations needed to achieve self-consistency. When SIMS measurements did not reach all the way to $x = \alpha+4\lambda_1$, they usually extended to at least $\alpha+2.5\lambda_1$, which proved adequate for nonlinear fitting to extract λ_1, b_1 and Z.

The shallow boundary α of the λ_1 region was determined as follows. The contour of the ^{18}O concentration immediately after the peak grades smoothly into the λ_1 region. To delineate a specific boundary in reproducible way, a curvature parameter κ was computed. The parameter quantifies how sharply a function y bends,[2–4] and is conventionally defined as

$$\kappa = \frac{|y''|}{(1+y'^2)^{\frac{3}{2}}} \quad \text{(S3)},$$

where y' and y'' respectively denote the first and second derivatives of y. Normally κ is constructed to lie in the range $0 < \kappa < 10$. As κ is dimensionless, reaching this range implies that y and x should nondimensionalized to have comparable magnitudes. Concentrations C were normalized by the natural abundance level of ^{18}O

$$y = \frac{C}{C_O} \quad \text{(S4)},$$

and depths x were normalized by the spacing Δx between SIMS concentration measurements

$$X = \frac{x}{\Delta x} \quad \text{(S5).}$$

These derivatives were calculated using seven-point central difference formulae according to:

$$y' = \frac{y_{i+3} - y_{i-3}}{6\Delta X} \quad \text{(S6)}$$

$$y'' = \frac{y_{i+3} - 2y_i + y_{i-3}}{9\Delta X^2} \quad \text{(S7)}$$

where i corresponds to a particular data point with nearest neighbors $i\pm1$ and third nearest neighbors $i\pm3$. With these definitions, we found empirically that requiring $\kappa < 0.02$ reliably identified a value of α suitable for setting the shallow end of the λ_1 region.

As mentioned earlier, SIMS measurements usually terminated at depths much shallower than λ_2. However, with α, λ_1, b_1, and Z known, λ_2 and b_2 could be determined mathematically by requiring continuity at the boundary between the λ_1 and λ_2 regions of both the profile itself and its first derivative. We consistently set this boundary at a depth equal to $\alpha+4\lambda_1$, where the spillover contribution attributable to residual λ_1 decay is at most about 8% of the contribution attributable to λ_2 decay. Requiring continuity of the profile itself at $\alpha+4\lambda_1$ means setting Eq. (S1) equal to Eq. (S2) at $x = \alpha+4\lambda_1$ to yield

$$ln\left[e^{\frac{-\alpha-4\lambda_1}{\lambda_1}+b_1} + \frac{C_O(Z-1)}{(C_{OT}-C_O)}\right] = \frac{-\alpha-4\lambda_1}{\lambda_2} + b_2 \quad \text{(S8).}$$

Requiring continuity of the first derivative yields

$$\frac{1}{\lambda_1} e^{-\frac{x}{\lambda_1}+b_1} = \frac{1}{\lambda_2} e^{-\frac{x}{\lambda_2}+b_2} \quad \text{(S9).}$$

Simultaneous solution of Eqs. (S8) and (S9) yields

$$\lambda_2 = \lambda_1\left[1 + \frac{C_O(Z-1)}{(C_{OT}-C_O)} e^{\frac{\alpha}{\lambda_1}+4-b_1}\right] \quad \text{(S10).}$$

Substitution of this value of λ_2 back into either Eq. (S8) or (S9) yields b_2.

The net flux F_{18} was computed as

$$F_{18} = N_{18}/t \quad \text{(S11),}$$

where N_{18} denotes the number of injected ^{18}O atoms. N_{18} was computed as the integral of $(C\text{-}C_O)$ throughout the entire solid. This integral was performed piecewise. The number N_{VP} of injected ^{18}O atoms appearing in the valley-peak region between $x = 0$ and α was obtained by numerical trapezoidal-rule integration of $(C\text{-}C_O)$. For $x > \alpha$, contributions to the integral from the λ_1 and λ_2 regions of the profile were computed analytically using Eq. (S1) and (S2) for C together with the

parameters λ_1, λ_2, Z, b_1 and b_2 determined as described above. The number of atoms in the λ_1 region, $N_{\lambda 1}$, is

$$N_{\lambda 1} = \int_{\alpha}^{\alpha+4\lambda 1} \left[C_O \left[\frac{C_{OT}-C_O}{C_O} \left(e^{-\frac{x}{\lambda_1}+b_1} \right) + Z \right] - C_O \right] dx \quad \text{(S12)},$$

while the corresponding number $N_{\lambda 2}$ in the λ_2 region is

$$N_{\lambda 2} = \int_{\alpha+4\lambda_1}^{\infty} \left[C_O \left[\frac{C_{OT}-C_O}{C_O} \left(e^{-\frac{x}{\lambda_2}+b_2} \right) + 1 \right] - C_O \right] dx \quad \text{(S13)}.$$

Performing the analytical integration and adding all the piecewise components together yields:

$$N_{18} = N_{VP} + N_{\lambda 1} + N_{\lambda 2} = N_{VP} + \left((C_{OT} - C_O) \left\{ \left[\lambda_1 e^{\frac{-\alpha}{\lambda_1}+b_1} (1 - e^{-4}) \right] + \left[\lambda_2 e^{\frac{-\alpha-4\lambda_1}{\lambda_2}+b_2} \right] \right\} \right) + 4\lambda_1 C_O (Z-1) \quad \text{(S14)}.$$

2. Statistical Analysis Example Calculation

The t-test calculations can be illustrated by comparing the flux (F_{18}) for Cases I and II, whose fluxes are closest together. The values of s_Δ (pooled variance), the t-statistic t, and the degrees of freedom (df) are:

$$s_\Delta = \sqrt{\frac{\sigma_{III}^2}{n_{III}} + \frac{\sigma_{IV}^2}{n_{IV}}} = 3.15 \times 10^{10}\ cm^{-2}s^{-1} \quad \text{(S15)}$$

$$t = \frac{\overline{F_{III}} - \overline{F_{IV}}}{s_\Delta} = 1.35 \quad \text{(S16)}$$

$$df = \frac{\left(\frac{\sigma_{III}^2}{n_{III}} + \frac{\sigma_{IV}^2}{n_{IV}} \right)^2}{\frac{\left(s_{III}^2/n_{III}\right)^2}{n_{III}-1} + \frac{\left(s_{IV}^2/n_{IV}\right)^2}{n_{IV}-1}} = 20.5 \quad \text{(S17)}$$

Use of statistical software or a t-table yields $p = 0.19$. Mann-Whitney U-tests tests were performed using the MATLAB function ranksum.

3. Adsorption Models

Definitions:

x = fraction of O originating from H_2O (includes both isotopes)

$(1–x)$ = fraction of O originating from O_2 (includes both isotopes)

F_{18} (F_{16}) = time-averaged net injection flux of ^{18}O (^{16}O)

F_W = time-averaged net injection flux of O if only water supplies O (linear proportion model)

k_{inj} = 1st order rate constant for O injection

$\theta_{OH,18}$ ($\theta_{OH,16}$) = surface coverage of OH labeled with ^{18}O (^{16}O)

θ_{OH} = total surface coverage of adsorbed OH

k_{AW} = adsorption rate constant for dissociative adsorption of water on TiO_2

k_{AO2} = adsorption rate constant for dissociative adsorption of O_2 on TiO_2

$Y_{18,W}$ ($Y_{16,W}$) = isotopic mole fraction of ^{18}O (^{16}O) in the water

$Y_{18,O2}$ ($Y_{16,O2}$) = isotopic mole fraction of ^{18}O (^{16}O) in the O_2

$C_{W,18}$ ($C_{W,16}$) = concentration (mol/l) of water labeled with ^{18}O (^{16}O) in the liquid phase

C_W = total concentration (mol/l) of water (all isotopes) in the liquid phase

$C_{O2,18}$ ($C_{O2,16}$) = concentration of dissolved $^{18}O_2$ ($^{16}O_2$) in the liquid phase (mol/l)

X_{O2} = chemical mole fraction of O_2 (all isotopes) in the gas phase

C_{O2} = total concentration (mol/l) of dissolved O_2 (all isotopes) in the liquid phase

$C_{O2,atm}$ = concentration of dissolved O_2 (all isotopes) at atmospheric pressure (mol/l)

R_{ads} = generic adsorption rate from the liquid phase to create OH on the surface

R_{des} = generic desorption rate into the liquid phase to remove OH from the surface

3.1 Linear Proportion Model

This model assumes that H_2O and O_2 contribute O and isotopic labels in linear proportion to their respective concentrations. A fraction x of O originates from H_2O, and a fraction $(1–x)$ originates from O_2. A mass balance on ^{18}O then yields:

$$F_{18} = Y_{18,W} x F_W + Y_{18,O2} X_{O2} (1 - x) F_W \qquad \text{(S18)}.$$

Equation (S18) assumes constant flux, neglecting the modest increase in surface annihilation (decrease in flux) that occurs with increasing time, and assumes the validity of Henry's law, where

the O_2 solubility is proportional to its partial pressure. Equation (S18) also implicitly assumes that ^{18}O injection and diffusion into TiO_2 occurs by two independent pathways (H_2O, O_2) with no chemical interactions. Linear regression on the four equations ($F_{18,I}$ - $F_{18,IV}$) and two unknowns (x, F_W) yields $F_W = 2.5\times10^{12}$ cm^{-2}s^{-1} and $x = 0.78$, with a total residual variance of 1.9×10^{22} cm^{-4}s^{-2}.

3.2 Dual Pathway Model

This model assumes that both H_2O and O_2 react through the same OH_{ads} intermediate species atop rutile TiO_2(110). Langmuir kinetics, constant flux, and the validity of Henry's law are all assumed. A mass balance on the rates of species exchange between the solid surface and fluid yields θ_{OH}. The calculation begins with the following rates:

$$R_{ads} = (k_{AW}C_W + k_{AO2}C_{O2})(1 - \theta_{OH}) \quad \text{(S19)}$$

$$R_{des} = (k_{dW} + k_{dO2})\theta_{OH} \quad \text{(S20).}$$

With the assumption of steady state, the mass balance is $R_{ads} = R_{des}$, or:

$$(k_{AW}C_W + k_{AO2}C_{O2})(1 - \theta_{OH}) = (k_{dW} + k_{dO2})\theta_{OH} \quad \text{(S21).}$$

Rearrangement yields θ_{OH}:

$$\theta_{OH} = \left[\frac{(k_{AW}C_W + k_{AO2}C_{O2})}{(k_{AW}C_W + k_{AO2}C_{O2} + k_{dW} + k_{dO2})}\right] \quad \text{(S22).}$$

Separation into two isotopic components and $\theta_{OH,18}$ and $\theta_{OH,16}$ begins with the substitutions $C_W = C_{W,16} + C_{W,18}$ and $C_{O2} = C_{O2,16} + C_{O2,18}$:

$$\theta_{OH} = \left[\frac{k_{AW}(C_{W,16} + C_{W,18}) + k_{AO2}(C_{O2,16} + C_{O2,18})}{(k_{AW}C_W + k_{AO2}C_{O2} + k_{dW} + k_{dO2})}\right] \quad \text{(S23)}$$

$$= \left[\frac{(k_{AW}C_{W,18} + k_{AO2}C_{O2,18})}{(k_{AW}C_W + k_{AO2}C_{O2} + k_{dW} + k_{dO2})}\right] + \left[\frac{(k_{AW}C_{W,16} + k_{AO2}C_{O2,16})}{(k_{AW}C_W + k_{AO2}C_{O2} + k_{dW} + k_{dO2})}\right] \quad \text{(S24).}$$

Substitution of the mole fractions $C_{W,18} = Y_{18,W}C_W$, $C_{W,16} = Y_{16,W}C_W$, $C_{O2,18} = Y_{18,O2}C_W$, and $C_{O2,16} = Y_{16,O2}C_W$ yields:

$$\theta_{OH} = \left[\frac{(Y_{18,W}k_{AW}C_W + Y_{18,O2}k_{AO2}C_{O2})}{(k_{AW}C_W + k_{AO2}C_{O2} + k_{dW} + k_{dO2})}\right] + \left[\frac{(Y_{16,W}k_{AW}C_W + Y_{16,O2}k_{AO2}C_{O2})}{(k_{AW}C_W + k_{AO2}C_{O2} + k_{dW} + k_{dO2})}\right] \quad \text{(S25).}$$

The first set of terms in brackets corresponds to $\theta_{OH,18}$ and the second set to $\theta_{OH.16}$, so:

$$\theta_{OH,18} = \left[\frac{(Y_{18,W}k_{AW}C_W + Y_{18,O2}k_{AO2}C_{O2})}{(k_{AW}C_W + k_{AO2}C_{O2} + k_{dW} + k_{dO2})}\right] \quad \text{(S26a)}$$

$$\theta_{OH,16} = \left[\frac{(Y_{16,W}k_{AW}C_W + Y_{16,O2}k_{AO2}C_{O2})}{(k_{AW}C_W + k_{AO2}C_{O2} + k_{dW} + k_{dO2})}\right] \quad \text{(S26b).}$$

Note that $\theta_{OH,18} + \theta_{OH,16} = \theta_{OH}$. Under water, one can assume $\theta_{OH} \approx 1$. Under such conditions, Eq. (S23) suggests $k_{dW} + k_{dO2} << k_{AW}C_W + k_{AO2}C_{O2}$, which implies that:

$$\theta_{OH,18} = \left[\frac{(Y_{18,W}k_{AW}C_W + Y_{18,O2}k_{AO2}C_{O2})}{(k_{AW}C_W + k_{AO2}C_{O2})}\right] \quad \text{(S27).}$$

Use of $C_{O2} = X_{O2}C_{O2,atm}$ yields:

$$\theta_{OH,18} = \left[\frac{(Y_{18,W}k_{AW}C_W + Y_{18,O2}X_{O2}k_{AO2}C_{O2,atm})}{(k_{AW}C_W + X_{O2}k_{AO2}C_{O2,atm})}\right] \quad \text{(S28).}$$

The rate of ^{18}O injection is therefore:

$$F_{18} = k_{inj}\theta_{OH,18} = k_{inj}\left[\frac{(Y_{18,W}k_{AW}C_W + Y_{18,O2}X_{O2}k_{AO2}C_{O2,atm})}{(k_{AW}C_W + X_{O2}k_{AO2}C_{O2,atm})}\right] \quad \text{(S29).}$$

A fraction x originates from the H_2O phase, and the remaining fraction $(1–x)$ from the gas phase:

$$x = \frac{k_{AW}C_W}{k_{AW}C_W + k_{AO2}C_{O2,atm}} \quad \text{(S30a)}$$

$$1 - x = \frac{k_{AO2}C_{O2,atm}}{k_{AW}C_W + k_{AO2}C_{O2,atm}} \quad \text{(S30b).}$$

Substitution of Eqs. (S30a) into Eq (S28) and rearranging yields:

$$\theta_{OH,18} = \frac{Y_{18,W}x + X_{O2}Y_{18,O2}(1-x)}{x + X_{O2}(1-x)} \quad \text{(S31a).}$$

A similar set of steps for $\theta_{OH,16}$ yields:

$$\theta_{OH,16} = \frac{Y_{16,W}x + X_{O2}Y_{16,O2}(1-x)}{x + X_{O2}(1-x)} \quad \text{(S31b),}$$

although it is also true that $\theta_{OH,16} = 1 - \theta_{OH,18}$ with the assumption of $\theta_{OH} \approx 1$ employed above. The injected fluxes are therefore:

$$F_{18} = k_{inj}\theta_{OH,18} = k_{inj}\left[\frac{Y_{18,W}x + X_{O2}Y_{18,O2}(1-x)}{x + X_{O2}(1-x)}\right] \quad \text{(S32a)}$$

$$F_{16} = k_{inj}\theta_{OH,16} = k_{inj}\left[\frac{Y_{16,W}x + X_{O2}Y_{16,O2}(1-x)}{x + X_{O2}(1-x)}\right] \quad \text{(S32b).}$$

In the asymptotic limit of $x \rightarrow 1$, Eq. (S18) from the linear proportion model represents a limiting case of Eq. (S32a) from the dual pathway model, with $F_W = k_{inj}$. Formally, the condition of $x = 0$ and $X_{O2} = 1$ leads to the same equivalence but makes no physical sense because experimentally, H_2O is always present to contribute some of the injected O.

Nonlinear regression for four cases ($F_{18,I}$ - $F_{18,IV}$) yields $x = 0.76$ and $k_{inj} = 2.2\times10^{12}$ $cm^{-2}s^{-1}$. From the best-fit value for k_{inj}, we can estimate $\theta_{OH,18}$ and $\theta_{OH,16}$ in one of two ways. One method divides individual values of F_{18} and F_{18} by the fitted value of k_{inj} to obtain corresponding "fitted" values of $\theta_{OH,18}$ and $\theta_{OH,16}$ according to the first equalities in Eqs. (S32a) and (S32b). The other method uses the chosen isotopic mole fractions in gas and liquid, the gas mole fraction of O_2, and the best-fit value of x to obtain theoretical "ideal" values of $\theta_{OH,18}$ and $\theta_{OH,16}$ according to Eqs. (S31a) and (S31b). Table S1 shows the corresponding values for the present experiments.

Table S1. Surface coverages of ^{18}O and ^{16}O

	Case I	**Case II**	**Case III**	**Case IV**
$\boldsymbol{\theta_{OH,18}}$ (fitted)	0.073	0.055	0.14	0.23
$\boldsymbol{\theta_{OH,18}}$ (ideal)	0.10	0.076	0.094	0.23
$\boldsymbol{\theta_{OH,16}}$ (fitted)	0.93	0.94	0.86	0.77
$\boldsymbol{\theta_{OH,16}}$ (ideal)	0.90	0.92	0.91	0.77

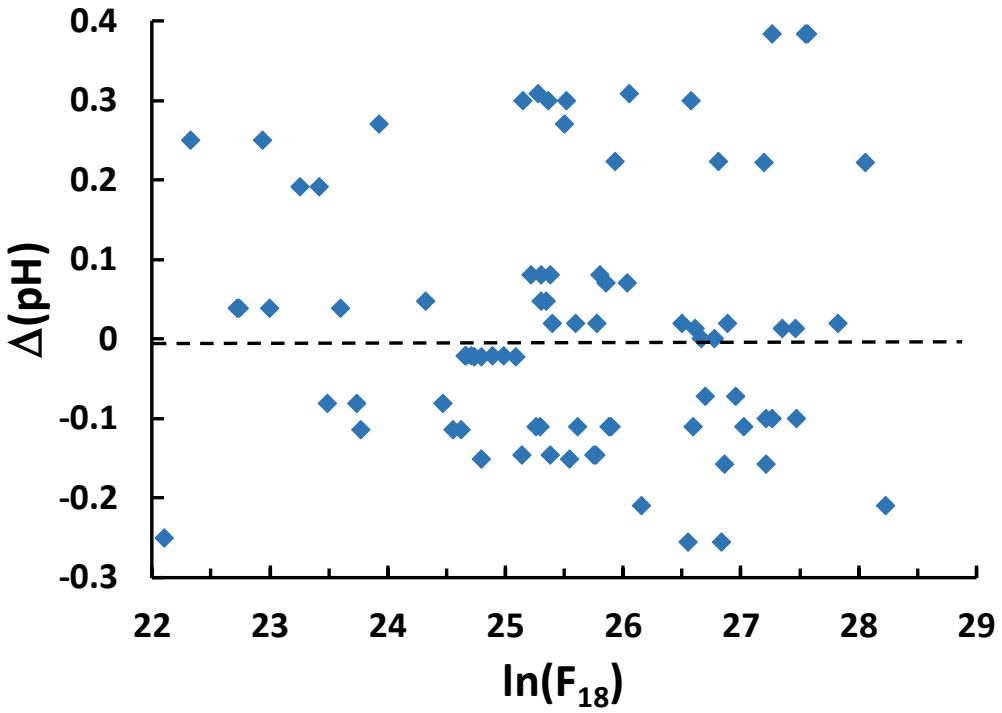

Figure S1. Change in solution pH measured at the start and end of the diffusion experiment as a function of the flux (F_{18}) of injected ^{18}O. The pH of the solution does not correlate with F_{18}. Whenever more than one profile was measured for a given specimen resulting in multiple values for F_{18}, the same pH change is plotted for all the values of F_{18}. This resulted in obvious discretization that is apparent for some values of ΔpH.

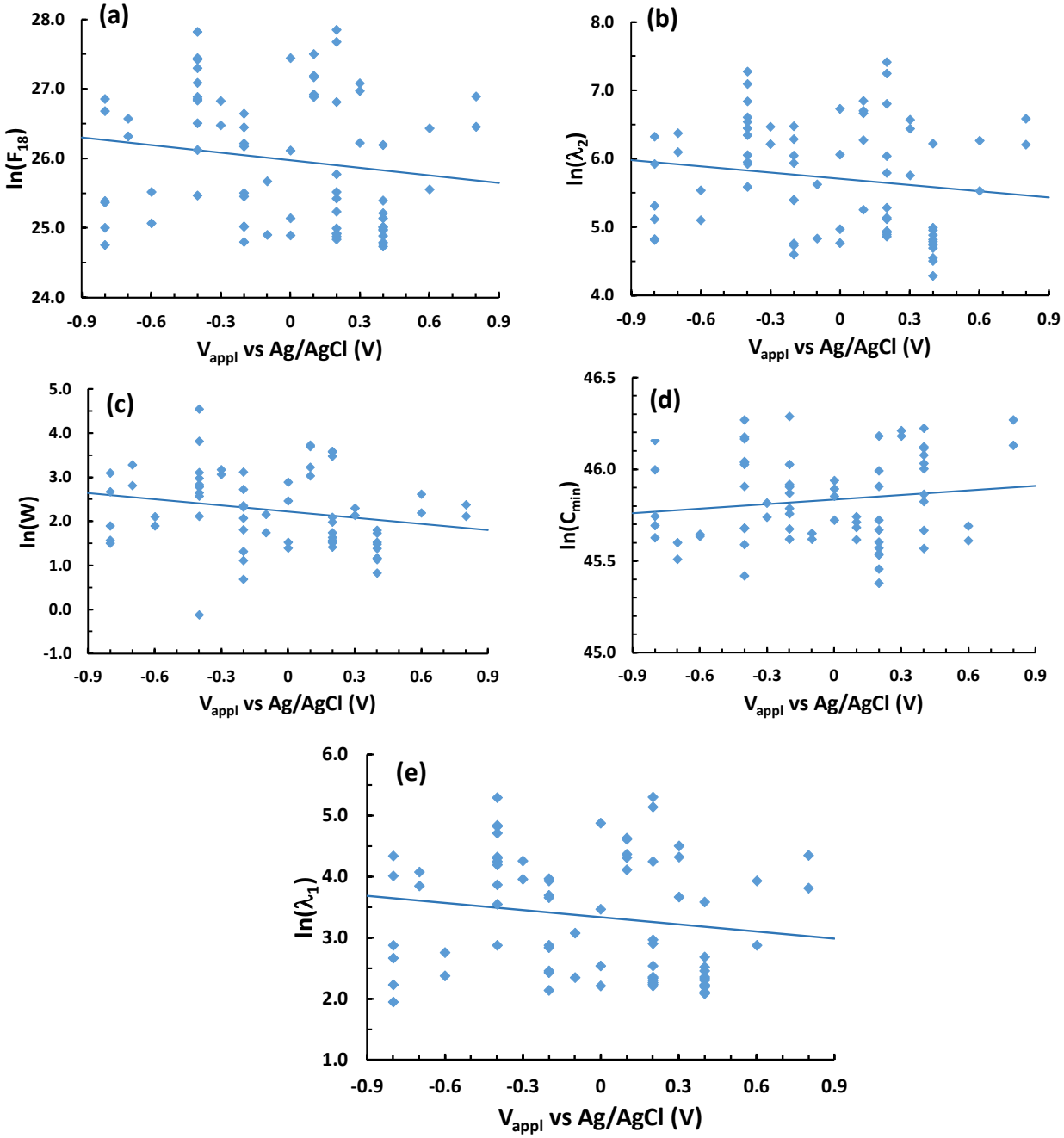

Figure S2. Profile metrics vs applied potential bias V_{appl} including (a) F_{18}, (b) λ_2, (c) W, (d) C_{min} and (e) λ_1 at 70°C. Lines represent linear least squares fits. For all data here, the water (10 at % ^{18}O) contained no electrolyte. The plots have nonzero slopes. Table S2 below reports the results of F-tests to determine whether the nonzero slopes represent statistical departures from zero (the null hypothesis). For all but W, the likelihood of the null hypothesis (p-value) is 0.15-0.25, which is generally considered too large for the slopes to be accounted statistically significant. For W, the p-value of 0.08 is noticeably smaller. Although F-tests are rather robust to deviations from normality,[5,6] we do not claim statistical significance, especially because the liquid and solid TiO_2 are both insulating and provide no mechanism for V_{appl} to exert an effect.

Table S2. Slopes of profile metrics vs V_{appl}: F-tests for null hypothesis*

Metric	Slope	Degrees of Freedom	F	p
F_{18}	-0.36±0.26	72	1.83	0.18
W	-0.47±0.25	66	3.24	0.08
C_{min}	0.08±0.07	66	1.33	0.25
λ_1	-0.39±0.27	72	2.01	0.16
λ_2	-0.30±0.23	72	1.77	0.19

*Statistical tests were performed on metrics after transformation to a natural logarithmic scale.

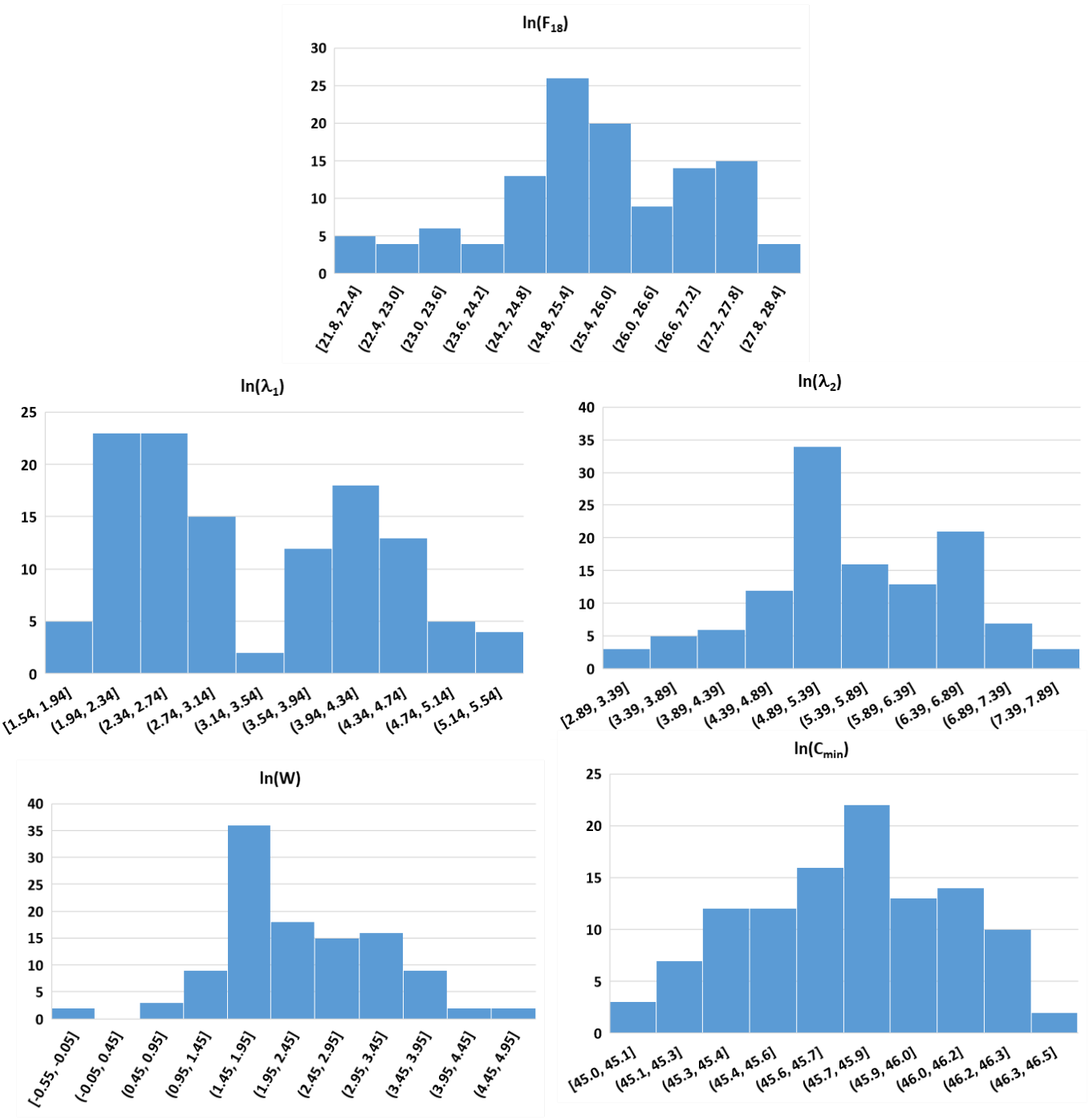

Figure S3: Histograms of the five different profile metrics at 70°C with applied bias. Some of the histograms are roughly normal (Gaussian) but others are clearly not. This figure (and S4) employs logarithmic plotting of all metrics because statistical analysis after logarithmic transformation is a well-established method[7,8] for improving the skewness of a data set by attenuating departures from the mean at the upper end of the range and amplifying them at the lower end. Logarithmic transformation is akin to working with solution pH rather than hydronium ion concentration.

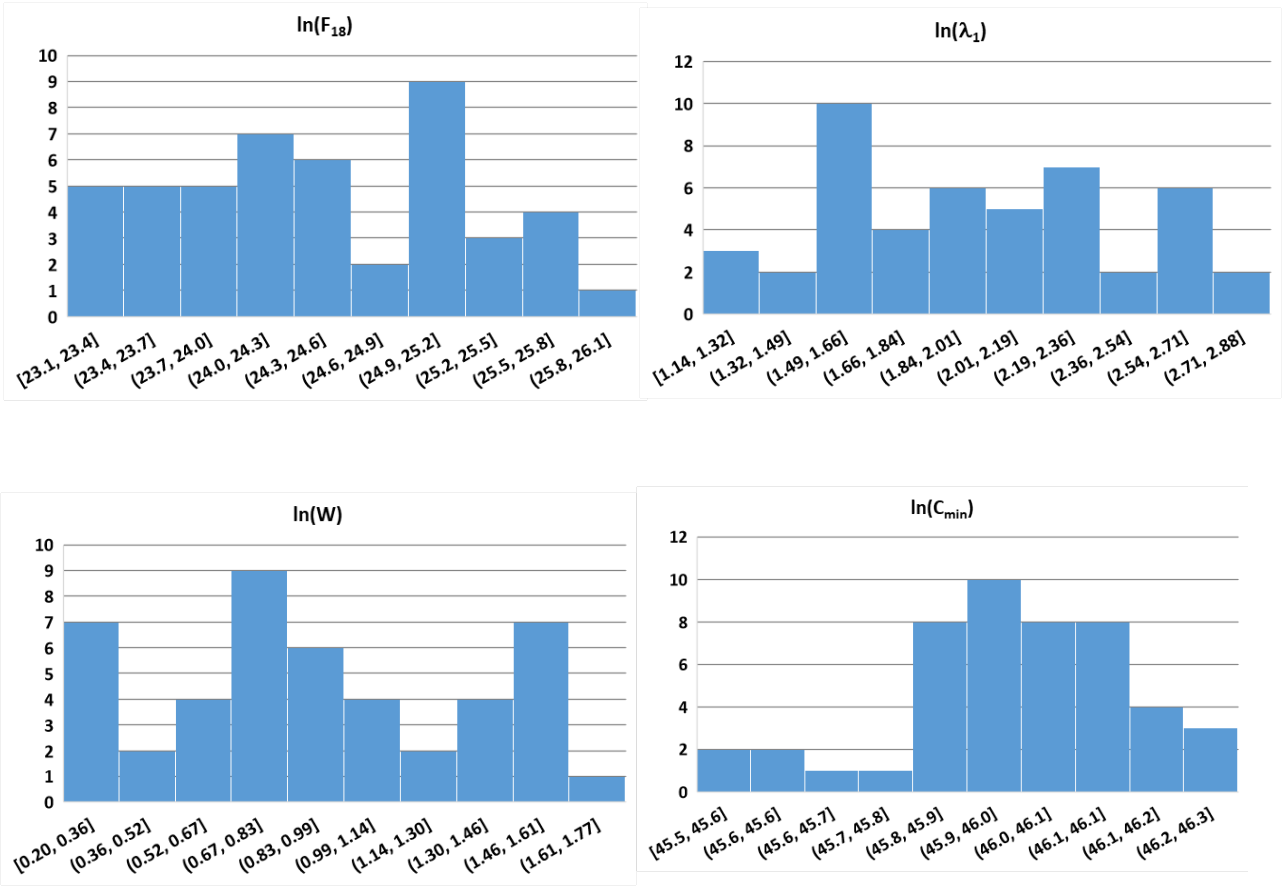

Figure S4: Histograms of the profile metrics for water without applied bias. Data were originally taken in the range 30-80°C as described previously,[9] and transformed to a single temperature of 70°C according to Arrhenius linear regression as described in Ref. [9]. For water without applied bias, profiles exhibited no counterpart to the λ_2 region elicited by applied bias. Some of the histograms are roughly normal (Gaussian), but others are clearly not.

Either with or without applied bias, non-normal distributions arise partly because the assumption of complete independence does not hold for all data. For water without applied bias, Ref. [9] reported that metrics measured at different points on a given specimen clustered together more closely than for different specimens. Similar clustering occurred here with applied bias, with the distributions at 70 °C affected by heavily sampled specimens at +0.2V and ±0.4V. In both cases, the diameter of the region sampled by SIMS was about 1 mm. For W and C_{min}, additional systematic bias arises because a few profiles exhibited fractionation that did not reach below natural abundance. These profiles are not included because no fractionation metrics can be determined using the definitions employed here.

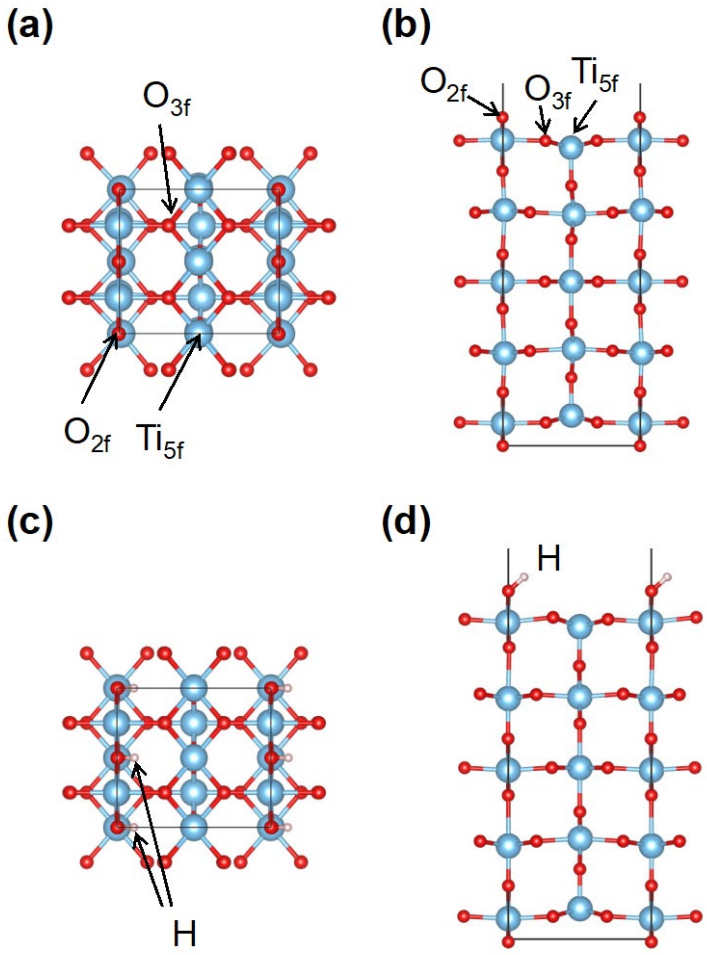

Figure S5. Atomic geometry of (a,b) pristine TiO_2(110) terrace and (c,d) adsorbed bridging hydroxyl. (a,c) show top views and (b,d) show side views. Shading colors respectively represent blue for Ti, red for O, and white for H.

Table S3. Adsorption energy and Bader charge of adsorbed O on TiO_2(110): Ti-rich conditions

TiO_2(110) surface conditions	Adsorption configuration	Adsorption energy (eV)		Bader charge (e^-)		Charge state
		E_F=0 eV	E_F=3.1 eV	adsorbed O atom	neighboring O atom	
Pristine	Dumbbell	6.23	6.23	-0.43	-0.69	0
	Split	6.38	0.32	-1.11	-0.94	-2
	On-top	8.06	5.03	-0.61	-1.09	-1
Bridging hydroxylated	Dumbbell	5.91	5.91	-0.54	-0.71	0
	Split	5.13	-0.93	-1.12	-1.03	-2
	On-top	3.22	0.20	-0.87	-1.13	-1

4. References

1 P. Gorai, A. G. Hollister and E. G. Seebauer, Measurement of defect-mediated oxygen self-diffusion in metal oxides, *ECS Journal of Solid State Science and Technology*, 2012, **1**, Q21–Q24.

2 F. Mokhtarian and A. K. Mackworth, A theory of multiscale, curvature-based shape representation for planar curves, *IEEE Trans Pattern Anal Mach Intell*, 1992, **14**, 789–805.

3 R. Goldman, Curvature formulas for implicit curves and surfaces, *Comput Aided Geom Des*, 2005, **22**, 632–658.

4 D. A. Walker, E. K. Leitsch, R. J. Nap, I. Szleifer and B. A. Grzybowski, Geometric curvature controls the chemical patchiness and self-assembly of nanoparticles, *Nat Nanotechnol*, 2013, **8**, 676–681.

5 M. J. Blanca, R. Alarcón, J. Arnau, R. Bono and R. Bendayan, Datos no normales: ¿es el ANOVA una opción válida?, *Psicothema*, 2017, **29**, 552–557.

6 M. M. Ali and S. C. Sharma, Robustness to nonnormality of regression F-tests, *J Econom*, 1996, **71**, 175–205.

7 J. M. Bland, D. G. Altman and F. J. Rohlf, In defence of logarithmic transformations, *Stat Med*, 2013, **32**, 3766–3768.

8 D. Curran-Everett, Explorations in statistics: the log transformation, *Adv Physiol Educ*, 2018, **42**, 343–347.

9 H. Jeong and E. G. Seebauer, Effects of Ultraviolet Illumination on Oxygen Interstitial Injection from TiO2 under Liquid Water, *The Journal of Physical Chemistry C*, 2022, **126**, 20800–20806.